Research Article | Vol. 27, No. 13 | 24 Jun 2019 | OPTICS EXPRESS 18776
Optics EXPRESS

Tuning the exponential sensitivity of a bound-state-in-continuum optical sensor

SILVIA ROMANO,[1,*] GIANLUIGI ZITO,[2,*] SOFÍA N. LARA YÉPEZ,[1] STEFANO CABRINI,[3] ERIKA PENZO,[3] GIUSEPPE COPPOLA,[1] IVO RENDINA,[1] AND VITO MOCELLA[1]

[1]National Research Council IMM, Via Pietro Castellino, Naples, 80131, Italy
[2]National Research Council IBP, Via Pietro Castellino, Naples, 80131, Italy
[3]National Research Laboratory of Berkeley, Molecular Foundry, Berkeley, CA 94720, USA
[*]silvia.romano@na.imm.cnr.it, g.zito@ibp.cnr.it

Abstract: In this work, we investigate the evanescent field sensing mechanism provided by an all-dielectric metasurface supporting bound states in the continuum (BICs). The metasurface is based on a transparent photonic crystal with subwavelength thickness. The BIC electromagnetic field is localized along the direction normal to the photonic crystal nanoscale-thin slab (PhCS) because of a topology-induced confinement, exponentially decaying in the material to detect. On the other hand, it is totally delocalized in the PhCS plane, which favors versatile and multiplexing sensing schemes. Liquids with different refractive indices, ranging from 1.33 to 1.45, are infiltrated in a microfluidic chamber bonded to the sensing dielectric metasurface. We observe an experimental exponential sensitivity leading to differential values as large as 226 nm/RIU with excellent FOM. This behavior is explained in terms of the physical superposition of the field with the material under investigation and supported by a thorough numerical analysis. The mechanism is then translated to the case of molecular adsorption where a suitable theoretical engineering of the optical structure points out potential sensitivities as large as 4000 nm/RIU.

1. Introduction

Dielectric nanostructures able to confine the electromagnetic field at the nanoscale are subject of intense research, given the strong impulse that resonant photonic metasurfaces could provide to push farther the frontiers of light-matter interaction [1–5]. Recently, great attention has been focused on a novel family of nonradiating resonant states that can be supported in engineered all-dielectric metasurfaces and termed bound states in the continuum (BICs) [6–14]. BIC existence is an intriguing phenomenon firstly proved in quantum mechanics and then extensively studied in electronic and photonic structures [15–19]. These special modes possess an ideal infinite Q-factor characterized by vanishing resonance linewidth since can be completely decoupled from the continuum of propagating free-space radiation [20–22]. Surprisingly, experimental deviation from an ideal behavior due to unavoidable radiation loss channels (like scattering from imperfections and material absoprtion) permits a partial coupling to external radiation and actually makes BIC resonators among the most effective light-matter interaction platforms [23–26]. There are mainly two mechanisms of ideal decoupling from the continuum. The first stems from the suppression of radiation due to the symmetry of the BIC field arising in highly symmetric points of the reciprocal space and gives rise to so-called symmetry-protected BICs. The second one is based on the accidental decoupling due to the suitable tuning of a peculiar system parameter, which results in accidental nonradiating condition. In general, the nonradiating condition at the BIC is a topology induced property of the photonic phase due to the vortex-structured polarization revealed in the reciprocal space [15, 27]. At highly symmetric points, both symmetry-protection-based decoupling from continuum and accidental mechanisms might coexist in the same structure [23]. The latter have been proved to be highly robust against input beam collimation and nanostructure

#366932 https://doi.org/10.1364/OE.27.018776
Journal © 2019 Received 7 May 2019; revised 21 May 2019; accepted 24 May 2019; published 19 Jun 2019

Optics EXPRESS

extension in lasing applications [23] and surface-enhanced fluorescence microscopy [24]. Very recent advances of BIC phenomeon include electromagnetic multipole theory interpretation [28] and momentum space merging of multiple bound states [29]. Recently, in-plane symmetry breaking for engineering and tuning of quasi-BIC modes with designer architectures of photonic crystal slabs [30] and metasurfaces [31,32] have also been proposed and applied for hyperspectral biomolecular detection.

In our recent works [33,34], we studied the sensing capability of an all-dielectric and transparent photonic crystal nanoscale-thin slab (PhCS) supporting bound states in continuum. Since the light confined in the photonic nanostructure at the BIC has a significant fraction of power in the evanescent tail, the peak wavelength of the resonance is strongly affected by the refractive index (RI) of the external medium or by molecular adsorption in case of surface binding events. This trivially occurs because the effective index n_e of the mode, generally affected by the material cladding, is in this case a rapid function of the superstrate optical constant given the sub-wavelength thickness of the confining PhCS. This allowed us to realize a BIC-based sensor with high sensitivity to environment media variation. In addition, the linewidth of a resonance-based device affects its figure of merit (FOM), defined as the ratio between the sensitivity and the full width at half maximum (FWHM), which ultimately represents the capability to follow tiny changes in the environment RI, thus providing sensors with low values of limits of detection. Thanks to the high Q-factor associated to BIC resonant modes, our device's FOM reached values as large as 450 and was applied also for ultrasensitive bio-molecular detection, revealing the capability of detecting antigen/antibody bindings with superficial density as low as 0.2 molecules/μm^2 [33, 34]. The sensor architecture was easily implemented in the biological experimental environment since the BIC mode is localized along the direction normal to the PhCS with a field exponentially decaying in the material to detect, but totally delocalized in the PhCS plane, which favors versatile and multiplexing sensing schemes.

Herein, we further investigate the physics underlying the sensing mechanism reporting a theoretical and experimental study of the exponential-growth sensitivity curve in our BIC-based device. The exponential sensitivity behavior is explained in terms of the physical superposition of the field with the material under investigation and supported by a thorough numerical analysis. In particular, we explore the impact of the system symmetrization (substrate/PhCS/analyte) on the performance of the sensing mechanism. We theoretically find an exponential sensitivity curve leading to differential values of $\sim$ 660 nm/RIU in relevant biological dielectric ranges. We also investigate the tuning mechanism of the exponential sensitivity by considering the rate of symmetrization of the evanescent tails of the electromagnetic field, achieving a potential sensitivity as large as $\sim$ 4000 nm/RIU for values of cladding materials mimicking molecular binding of proteins or aminoacids. Finally, we validate the exponential-growth model of the resonance peak experimentally in certain ranges of RI.

2. Numerical modeling

We considered a dielectric geometry consisting of a square lattice of cylindrical air holes etched in a thin film of silicon nitride (Si_3N_4). This material is transparent in both visible and infrared ranges of light and has a real part refractive index of 2.15 at 532 nm [24]. A scheme of the resonator is shown in Fig. 1(a), where the PhCS unit cell is shown with bottom region made of quartz (SiO_2) of RI n_s, the coverslip experimentally supporting the silicon nitride layer of RI n_p, and the top material, initially air, then replaced with different cladding materials of RI n_c. The thickness of the unit cell slab is h, the lattice constant a, the hole radius r. The operating principle of the sensing scheme is the spectral shift of the peak wavelength λ_p of the quasi-BIC resonance as a function of the cladding n_c, as depicted in Fig. 1(b).

Numerical modeling was carried out using a rigorous coupled wave approach (RCWA) [35]

Optics EXPRESS

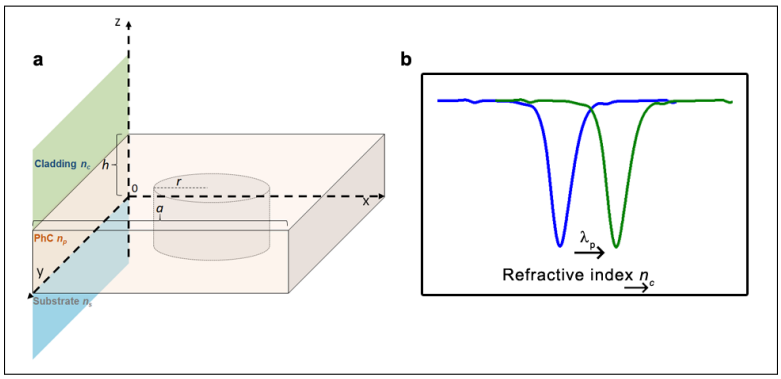

Fig. 1. (**a**) Layout of the PhCS unit cell. (**b**) Operating principle of the sensing scheme: the high Q resonance shifts as function of the cladding material due to density change of the homogeneous liquid cladding or molecular adsorption to the surface where the electromagnetic field is localized and amplified, thus increasing interaction of the molecules with light.

and finite element method (Comsol Multiphysics 5.2a) [36,37]. The $\mathbf{\Gamma}^{(2)}$ wavevectors, parallel to the (x, y)-plane of the PhCS, have all modulus $\beta_0 = 2\pi/a$, *i.e.* larger than the wavevector modulus both in SiO_2, given that $2\pi/a > 2\pi n/\lambda = k_{SiO_2}$, and air, given that $2\pi/a > 2\pi/\lambda = k_{air}$. Thus, at normal incidence the mode wavevector has a purely imaginary z-component in both regions of index n_s (1) and n_c (2), $k_z^{1,2} = \sqrt{k_{air,SiO_2}^2 - \beta_0^2} \doteq i\kappa_{1,2}$ and cannot couple to the far field. It is indeed exponentially decaying in both air and quartz, with a larger decay length in the glass since $\kappa_1 < \kappa_2$. The exponential evanescent decay is the condition that actually defines the transition from a confined mode totally decoupled from free-space radiation and leaky mode, having a non-null oscillatory behavior in the free space around the PhCS because of coupling to out-radiating modes. In Fig. 2(a), three types of TM-like BIC modes are displayed (numerically calculated for the parameters given in the inset), classified as irreducible representations of the symmetry group C_4v of $\mathbf{\Gamma}$ point [38]. While the first two are both singly-degenerate, symmetry-protected BICs, the third has a doubly-degenerate irreducible representation of type E, which is compatible with free-space radiation that has same representation at $\mathbf{\Gamma}$. In this case, decoupling from the continuum is due to the superposition of the two eigen-functions of the E representation that destructively interfere outside the slab. Figures 2(b) and 2(c) show the top and side view, respectively, of the field intensity in the unit cell, which demonstrates the local confinement with non-radiative character. All BIC modes have theoretically diverging Q-factors, regardless of their intrinsic symmetry properties.

In a real, finite structure, The BIC field can be seen as a TM mode propagating in the dielectric film along the symmetry directions imposed by the PhCS. As in planar waveguides, the imaginary wavevector component κ_2 is related to the propagation constant β. Changing the material cladding index n_c, *via* superficial molecular adsorption or a different RI liquid, affects both evanescent decay length and BIC peak wavelength λ_p due to the variation of the effective index $n_e = \beta/k_0$. Provided the BIC existence for a wide range of n_c values until confinement is hampered when n_c exceeds certain values (due to substrate leakage [39]) or is too close to n_p, once fixed n_p and n_s, it is possible to follow what happens to the BIC field as a function of n_c. As the optical contrast provided by the index mismatch $n_p - n_c$ between the PhCS and cladding reduces by increasing n_c, the BIC field profile across the normal to the surface becomes progressively more symmetric, as shown in Fig. 3(a) for the A_1 BIC mode, and with larger decay length δ as n_c approaches n_s. The growth of the decay length is actually an exponential function of n_c, as shown in Fig. 3(b).

Optics EXPRESS

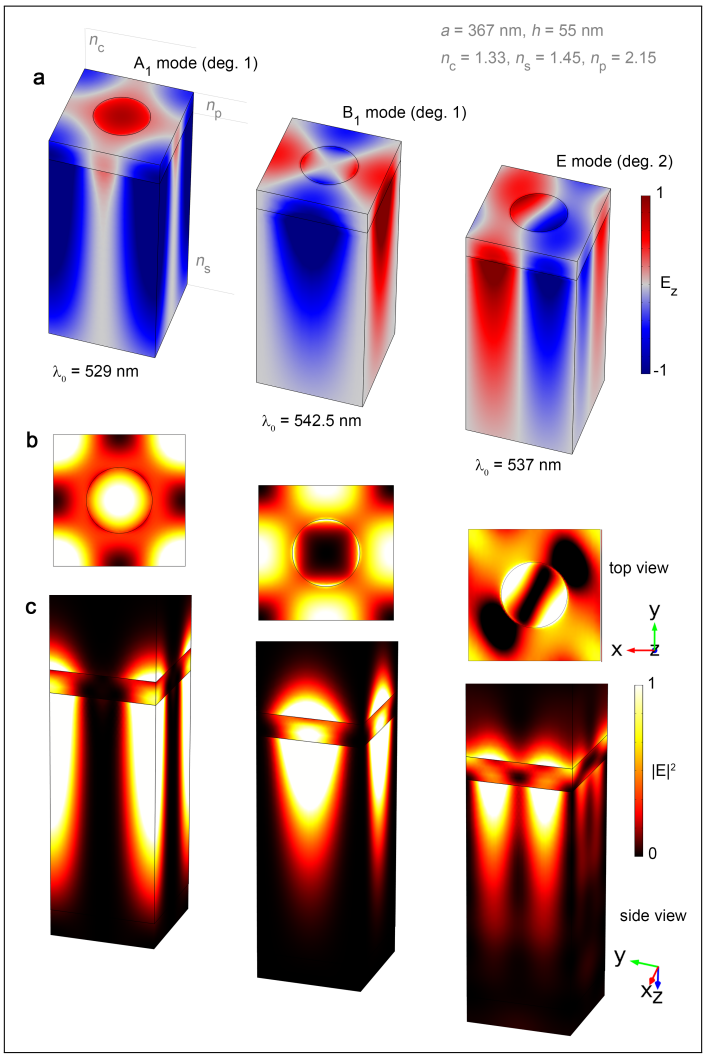

Fig. 2. (**a**) Representative TM-like mode profiles at **Γ** (C4v point group) in the unit cell, numerically calculated for the PhCS/liquid interface under consideration: two singly-degenerate symmetry-protected BICs of type A_1 and B_1, respectively, and a doubly-degenerate resonance-trapped BIC, classified as E-mode. (**b**) Top view of the electric field intensity in the unit cell. (**c**) Side view of the electric field intensity revealing the confinement and the evanescent character outside the structured film of index n_p.

A very similar behavior occurs for the other modes, since it stems from the evanescent tail decay depending on the optical contrast.

As a consequence, the fraction of optical energy in the cladding material progressively increases affecting the effective index of the BIC mode. The rate of variation of n_e (so does λ_p) depends on the same optical contrast with the cladding and is then proportional to the same n_e, which results in an exponentially increasing red shift of λ_p. Numerical simulations are depicted in Fig. 4.
In addition, we can expect that the rate of symmetrization of the evanescent tails (cladding *vs* substrate) of the electromagnetic field is affected by the phase mismatch between the substrate index n_s and PhCS material n_p. Therefore, a possible tuning parameter that can be adopted for

Optics EXPRESS

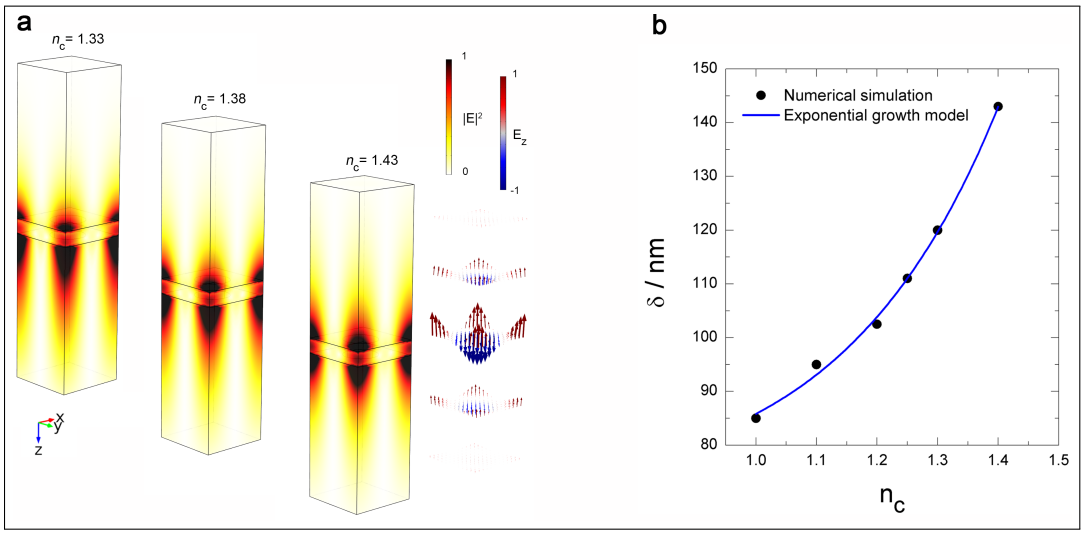

Fig. 3. (**a**) Symmetry increasing along z-axis of the A_1 type BIC field with progressively balanced evanescent tails in quartz substrate and liquid cladding (please note reversed color scale in $|E|^2$ for visualization clarity). The $\boldsymbol{E}$-field arrow map reveals a TM-like character with exponentially decreasing amplitude along z (colormap associated to the sign of E_z). (**b**) Exponential growth of the decay length δ of the evanescent tail in the liquid cladding when the cladding index n_c approaches the quartz substrate n_s = 1.45. The model fit (solid line) is given in Eq. (1).

modulating the exponential sensitivity of the optical sensor relies on $\Delta = n_p - n_s$. The lower Δ, the higher will be the rate of symmetrization, *i.e.* the rapidity to achieve a symmetric z cross section in the evanescent regions, and hence also the steepness of the exponential variation of the effective index n_e as a function of the cladding material n_c. This behavior is indeed shown in Fig. 4 for different values of Δ corresponding to progressively lower index mismatch between the PhCS material and substrate. Three examples are shown of the typical regimes that can be individuated depending on the parameters. We used the empirical equation model in Eq. (1) to fit the dependence of the peak wavelength λ_p with the parameters,

$$\lambda_p = \lambda_0 + \delta\lambda \exp\left[\alpha\left(\frac{n_c - n_0}{n_p - n_s}\right)\right], \tag{1}$$

which resulted in good agreement with the values obtained from FEM numerical simulations for parameters $\alpha \simeq 2$, $n_0 \simeq 1$, $\lambda_0 \simeq 524$ nm, $\delta\lambda \simeq 0.085$ nm. The same exponential growth model was used to fit the data in Fig. 3(b) and all the experimental results described in the following section. The behavior varies from an almost linear sensitivity curve to a steep exponential. In the last case, it is possible to achieve sensitivity as large as $\sim$ 400 nm/RIU in a biologically relevant range of values for n_c ranging between 1.52 and 1.55, as for macro-molecular binding. For increasing cladding refractive index up to 1.6, the theoretical sensitivity becomes 660 nm/ RIU (human *serum* albumin has a RI of 1.603, DNA of 1.583 [40]). Changing the design parameters can be useful to match a specific range of refractive index to maximize the response of the system. As for instance, the case $\Delta = 0.15$ has a faster variation of λ_p in a smaller range of n_c. In particular, in this case, when n_c reaches values of the order of 1.7 (as for instance, tubulin has a RI of 1.64, serine and glutamine 1.67, histidine 1.70, tryptophan 1.75 [40]), then the sensitivity increases of an order of magnitude and can be as large as $\sim$ 4000 nm/RIU.

For what concerns the possible thickness of the layer of high RI that can affect the sensitivity

Optics EXPRESS

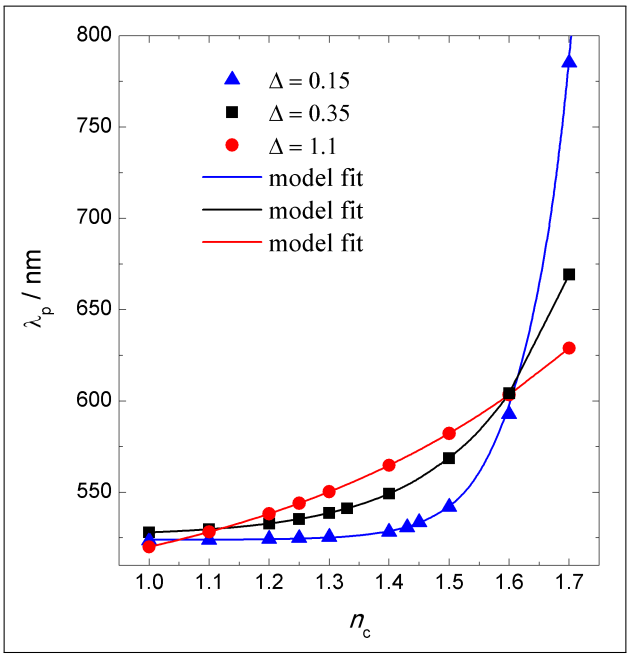

Fig. 4. (**a**) Exponential growth of λ_p as a function of the liquid cladding index n_c (B_1-mode) for fixed $n_s = 1.45$, and $n_p = n_s + \Delta$. Varying suitably the index mismatch $\Delta = n_p - n_s$ for feasible material parameters that allow BIC existence, it is possible to tune the sensitivity of the curve $\lambda_p(n_c)$ in specific ranges of RI for targeted applications, changing its character from a near linear behavior to a steep exponential curve. The points are numerically calculated results from FEM simulations, whereas the solid line is the model fit in Eq. (1).

of the system, it is worth to mention that the behavior of the resonance shift as a function of the layer thickness is profoundly different from that of an isolated dielectric nanoparticle in which the size effect rules the energy shift [41]. In case of the BIC, the mode behavior is collective and the coupling among unit cells determines the existence of the mode itself. In a recent paper, we experimentally and theoretically addressed the role of a thin molecular layer covering the PhC surface [33]. We also measured a good resonance shift even in case of bindings events with surface density of the order of 0.3 molecules/μm^2 [34]. The point is that the optical field is very large only close to the surface where the superposition with the material is maximum, therefore a thick layer of material does not appear to be necessary to induce a measurable energy shift, which is also consistent with the finding recently reported in [31], where a significant resonance energy shift was claimed for an adsorption density of only two molecules per unit cell. Therefore, sensitivity values of the order of ~ 4000 nm/RIU are strictly indicative of the bulk refractometric sensing performance but nonetheless can be seen as indicative of the potential sensitivity towards surface binding events.

The limitation of the approach here discussed is of course ruled by the existence of a BIC mode for the design parameters n_s, n_p, n_c. In this regard, the BIC point at $\mathbf{\Gamma}$ is a topological property of the photonic phases realized by this kind of dielectric geometry [22, 27], and as such it is robust against parameter tuning. Indeed the case $\Delta = 0.15$ is achieved with $n_p = 1.6$ and $n_s = 1.45$, a remarkably low dielectric contrast, which points out the possibility of using soft materials instead of silicon nitride for the PhCS layer, thus unveiling a brand new scenario of potential technological applications.

Optics EXPRESS

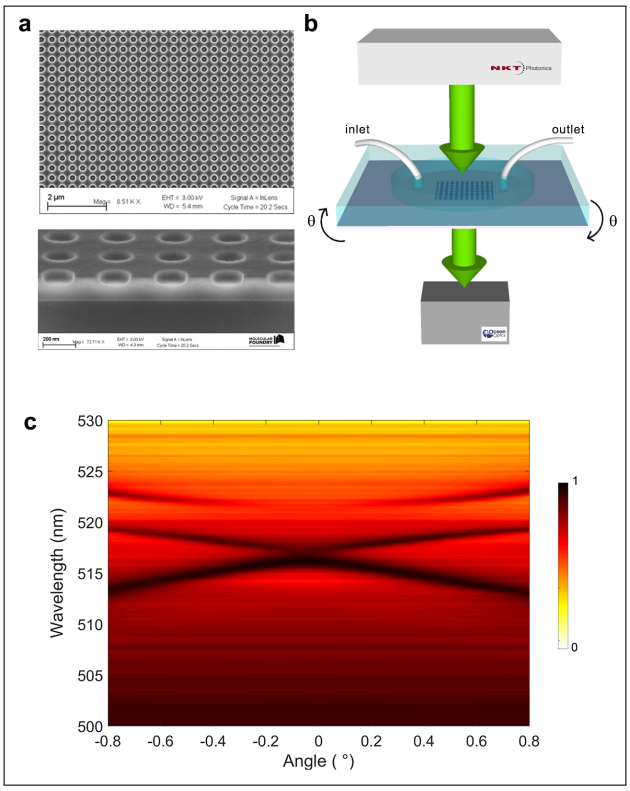

Fig. 5. (**a**) Scanning electron imaging micrographs of a characteristic sample. (**b**) Schematic layout of the PhCS integrated in the microfluidic chamber and basic characterization setup (input light is polarized with a Glan-Thompson polarizer); reflectance is obtained as $1 - T(\theta, \lambda)$. (**c**) Dispersion diagram along $\mathbf{\Gamma X}$ of the PhCS for $n_c = 1$. The three bands have theoretically vanishing linewidths approching $\theta = 0°$. Numerical simulations classify the top band mode as B_1 and the converging bands as E-type.

3. Experimental results

PhCMs of Si_3N_4 with an area of 1 mm^2 were fabricated by means of electron beam lithography and coupled plasma etching process. The holes square lattice parameters (lattice constant a, hole radius r, hole depth h, quartz substrate n=1.45) were optimized to realize platforms resonant at different wavelengths. Figure 5(a) shows a SEM image of a typical sample. In Fig. 5(b), a schematic layout of the characterization setup is shown. A representative dispersion diagram measured acquiring the reflectance $R(\lambda, \theta)$ as a function of the input angle θ for $n_c = 1$ (blank sensor with top cladding material of air) is shown in Fig. 5(c), in this case θ varies in the direction $\mathbf{\Gamma X}$. The actual height h was measured by atomic force microscopy and resulted typically 10% lower than designed value, which resulted in an experimental BIC mode of type E emerging at ~ 517 nm and type B_1 at 522.5 nm for n_c=1, a =367 nm, h = 55 nm, r = 90 nm.

The PhCS was then implemented with a polydimethylsiloxane (PDMS) microfluidic chamber to control the liquid infiltrated over the sensing surface (fabrication details are reported in [33]). The device was illuminated with a collimated supercontinuum laser source (SuperK NKT Photonics, range 480-2400 nm) in order to monitor the resonant peak shift as a function n_c infiltrating liquid of various RI. The measurements were performed in two different RI ranges, from 1.333 to 1.377 by using water/isopropyl alcohol solutions, and from 1.400 to 1.452 by using Cargille certified RI

Optics EXPRESS

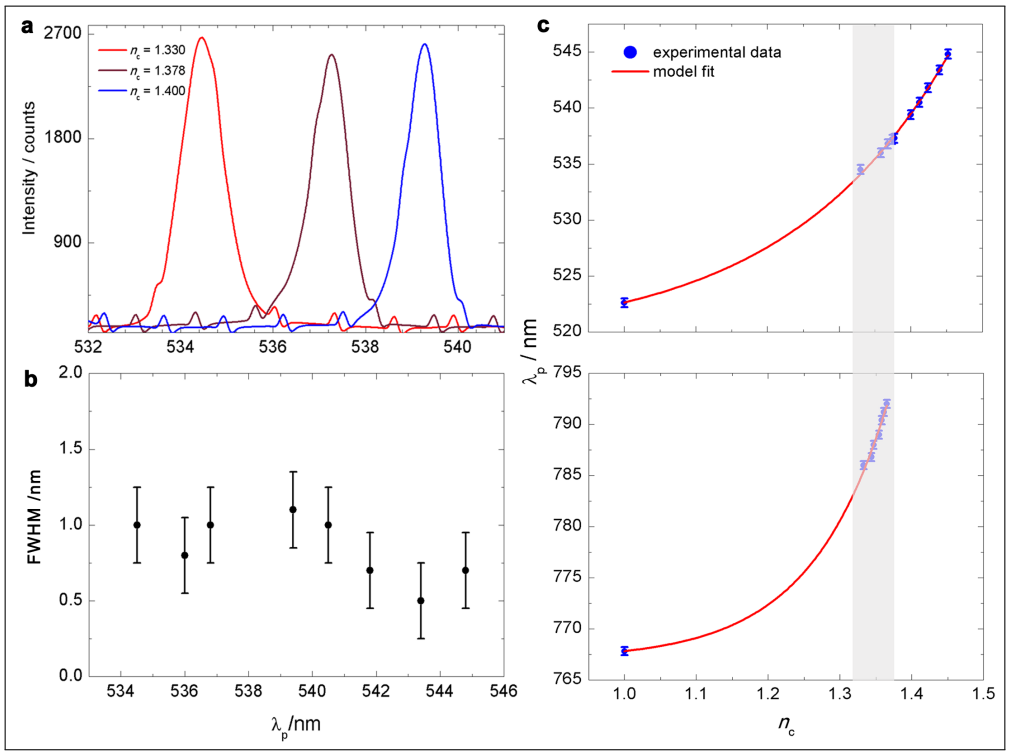

Fig. 6. (**a**) Representative resonance spectra in refractometric sensing for several cladding liquids. (**b**) FWHM of the resonant peak as a function of the spectral peak position. (**c**) Comparison of the exponential sensitivity curves of the resonant peak as a function of the cladding refractive index n_c for n_p = 2.215 (top panel) and n_p = 1.90 (bottom panel).

liquids. Each transmittance/reflectance spectrum was conveniently collected at normal incidence, although previous characterizations revealed angle-independent sensitivities [33]. The fluids were infiltrated with a syringe infusion pump (KD Scientific). The case reported in Figs. 6(a)-(c) refers to the BIC resonator in the visible range. Several representative resonance spectra are shown in Fig. 6(a). As shown in Fig. 6(b), experimentally, the FWHM of the resonant peak resulted nearly constant throughout all measurements for increasing RI, demonstrating the robustness of this refractometric sensing approach. Figure 6(c) (top panel) shows the peak wavelength evolution with n_c.

As mentioned above, the large spatial overlap between the nonradiating evanescent field and the surrounding fluid cladding due to the tight subwavelength confinement gives rise to a rapid function of the surrounding medium RI (Fig. 3). The penetration length of the field grows by increasing n_c, reaching a maximum value when the RI over the surface matches the substrate RI. The related exponential growth was experimentally confirmed as reported in Fig. 6(c) (top panel), where the resonant peak λ_p is plotted as a function of n_c. The solid line represents the empirical model fit in Eq. (1), in good agreement with the experimental points. The local sensitivity $\partial\lambda_p/\partial n_c|_{n_c=1.42}$ achieved with this PhCS for the RI variation explored was approximately ~ 103 nm / RIU. Ellipsometric characterization (Horiba Jobin Yvon, UV-IR range) of the silicon nitride film gave n_p = 2.215, *i.e.* for Δ = 0.765.

Given a nearly constant FWHM ≃ 0.8 nm [Fig. 6(b)], the FOM, defined as the ratio between sensitivity and FWHM of the resonant peak, was in the range of 129. It must be noted that the confinement associated to the BIC can actually decrease with increasing radiation leaking in

Optics EXPRESS

free-space for reduced values of the optical contrast among the PhCS and the liquid cladding. The initial resonance FWHM in air was indeed lower, approximately of 0.4 nm, denoting a higher $Q-$factor, and hence corresponded to a larger FOM of 258. However, the linewidth broadening is not detrimental to sensing application provided that the linewidth does not increase excessively, as reported in Fig. 6(b). The actual FOM reached in liquid defines more realistically the potential of the sensing device whose Q-factor is unavoidably reduced when in contact with highly concentrated solutions of analytes or high-index media.

A second set of measurements for reduced phase mismatch $\Delta = 0.45$ was carried out with a lower $n_p = 1.9$, keeping constant the substrate index, and is reported in the bottom panel of Fig. 6(c). In this case, the PhCS was designed for IR applications, and the measured value of $\partial\lambda_p/\partial n_c|_{n_c=1.38} \sim 226$ nm / RIU, *i.e.* the sensitivity increased of a factor ~ 2.2 by tuning one of the material parameter affecting Δ. This result demonstrates experimentally the possibility to increase the sensitivity of the BIC-based sensor, at least in certain range of RI with the aim of targeting specific bio-molecular applications. This was achieved by varying a simple material property and can be a general approach providing that the material parameters allow the existence and evolution of the BIC mode in the range of RI under analysis. Further research is still necessary however to access the steep exponential sensitivity theoretically predicted in Fig. 4. The experimental challenge is in this case determined by the film quality and homogeneity of a lower refractive index material, as for instance made of polymer.

As discussed in a previous paper [33], the IR resonator showed resonances with reduced FWHM varying from 0.4 nm in air to 0.6 nm at the higher RI of the cladding. We ascribed to the improved fabrication tolerance of the larger structure (see [33]), and inferior IR material absorption, the improved Q-factor. In this second case, the FOM started from a remarkable value of ~ 565 in air where the FWHM was 0.4 nm and reduced to 377 at the higher RI.

Given the constant FWHM, also the FOM behaves as an exponential-growth function of type given in Eq. (1) with n_c, which points out an excellent capability of following tiny changes of RI or material environment variation/fluctuation. From a technical point of view, the refractometric limit of detection (LOD) depends on the spectral resolution of the spectrometer, detector noise, acquisition scheme and data analysis approach [42]. Admitting a basic resolution of 0.01 nm, the LOD in our case is conservatively of the order of 4×10^{-5} RIU. Using advanced analysis data and suppressed noise detection [42], the spectral resolution can be of the order of 10^{-4} nm, which in our case then would correspond to a refractometric LOD of 4×10^{-7}. A fair comparison with typical refractometric resonators requires to consider the visible window in which our device operates, which may indeed facilitate sensing schemes in many applications, avoiding as for instance water absorption (large in IR) for water-based refractometric solutions. The LOD value must be then compared with the results that can be achieved with PhCS and/or nanocavities in the visible spectral window. In that case, the optical absorption of the materials typically employed, like crystalline silicon, actually hampers highly sensitive detection (10^{-2} RIU) because of very poor Q-factors [43]. On the other hand, in the IR range where silicon and plasmonic resonators are efficient, the bottleneck, as above mentioned, is water absorption. Nonetheless, high sensitivity of the order of ~ 1000 nm/RIU or more can be reached with SPP sensors. However, an interesting advantage provided by our device is the possibility of microscopy-based interrogation and transparency of the samples [33, 34].

4. Conclusion

Summarizing, we investigated the sensing mechanism provided by an optical sensor based on bound states in the continuum. The deep subwavelength metasurface is characterized by a BIC electromagnetic field localized along the normal direction and exponentially decaying in the material to detect. The mode is instead totally delocalized in the transverse plane over the

Optics EXPRESS

millimeter scale, which favors versatile and multiplexing sensing schemes. We explored the potential tuning of the sensitivity by addressing the physical transduction mechanism provided by the evanescent field. The physical superposition of the field with the material under investigation allows a good sensing performance as supported by a thorough numerical analysis. In particular, the tuning of the rate of symmetrization of the evanescent field as a function of the cladding optical constant (liquid material or adsorbed material under analysis) resulted promising to achieve potential sensitivities as large as 4000 nm/RIU. Experimentally, we verified the tuning possibility and observed an exponential sensitivity leading to differential values as large as 226 nm/RIU with excellent FOM. Based on our theoretical results, we foresee the possibility to enhance the sensing mechanism by changing the BIC-sensor material parameters towards lower dielectric contrast.

References

1. P. Genevet, F. Capasso, F. Aieta, M. Khorasaninejad, and R. Devlin, "Recent advances in planar optics: from plasmonic to dielectric metasurfaces," Optica **4**, 139–152 (2017).
2. A. E. Krasnok, A. E. Miroshnichenko, P. A. Belov, and Y. S. Kivshar, "All-dielectric optical nanoantennas," Opt. Express **20**, 20599–20604 (2012).
3. L. K. Ausman and G. C. Schatz, "Whispering-gallery mode resonators: Surface enhanced Raman scattering without plasmons," J. Chem. Phys. **129**, 054704 (2008).
4. M. Caldarola, P. Albella, E. Cortés, M. Rahmani, T. Roschuk, G. Grinblat, R. F. Oulton, A. V. Bragas, and S. A. Maier, "Non-plasmonic nanoantennas for surface enhanced spectroscopies with ultra-low heat conversion," Nat. Commun. **6**, 7915 (2015).
5. E. De Tommasi, A. Chiara De Luca, S. Cabrini, I. Rendina, S. Romano, and V. Mocella, "Plasmon-like surface states in negative refractive index photonic crystals," Appl. Phys. Lett. **102**, 081113 (2013).
6. J. von Neumann and E. P. Wigner, "Über merkwürdige diskrete Eigenwerte," Physikalische Zeitschrift **30**, 465–467 (1929).
7. C. Wei Hsu, B. Zhen, S.-L. Chua, S. G. Johnson, J. D. Joannopoulos, and M. Soljačić, "Bloch surface eigenstates within the radiation continuum," Light. Sci. & Appl. **2**, e84 (2013).
8. D. Marinica, a. Borisov, and S. Shabanov, "Bound States in the Continuum in Photonics," Phys. Rev. Lett. **100**, 183902 (2008).
9. M. I. Molina, A. E. Miroshnichenko, and Y. S. Kivshar, "Surface bound states in the continuum," Phys. Rev. Lett. **108**, 070401 (2012).
10. E. N. Bulgakov and A. F. Sadreev, "Bound states in the continuum in photonic waveguides inspired by defects," Phys. Rev. B - Condens. Matter Mater. Phys. **78**, 0751051 (2008).
11. R. Porter and D. V. Evans, "Embedded Rayleigh-Bloch surface waves along periodic rectangular arrays," Wave Motion **43**, 29–50 (2005).
12. E. Penzo, S. Romano, Y. Wang, S. Dhuey, L. Dal Negro, V. Mocella, and S. Cabrini, "Patterning of electrically tunable light-emitting photonic structures demonstrating bound states in the continuum," J. Vac. Sci. & Technol. B, Nanotechnol. Microelectron. Materials, Process. Meas. Phenom. **35**, 06G401 (2017).
13. B. Zhen, C. W. Hsu, L. Lu, a. D. Stone, and M. Soljačić, "Topological Nature of Optical Bound States in the Continuum," Phys. Rev. Lett. **113**, 257401 (2014).
14. S. Romano, S. Cabrini, I. Rendina, and V. Mocella, "Guided resonance in negative index photonic crystals: a new approach," Light. Sci. & Appl. **3**, e120 (2014).
15. C. W. Hsu, B. Zhen, A. D. Stone, J. D. Joannopoulos, and M. Soljacic, "Bound states in the continuum," Nat. Rev. Mater. **1** (2016).
16. V. Mocella and S. Romano, "Giant field enhancement in photonic resonant lattices," Phys. Rev. B - Condens. Matter Mater. Phys. **92**, 1–5 (2015).
17. E. N. Bulgakov and D. N. Maksimov, "Optical response induced by bound states in the continuum in arrays of dielectric spheres," *J. Opt. Soc. Am. B* **35**, 2443 (2018).
18. K. Koshelev, A. Bogdanov, and Y. Kivshar, "Meta-optics and bound states in the continuum," Sci. Bull. (2018).
19. K. Koshelev, G. Favraud, A. Bogdanov, Y. Kivshar, and A. Fratalocchi, "Nonradiating photonics with resonant dielectric nanostructures," Nanophotonics **8**, 725âĂŞ745 (2019).
20. Y. Plotnik, O. Peleg, F. Dreisow, M. Heinrich, S. Nolte, A. Szameit, and M. Segev, "Experimental Observation of Optical Bound States in the Continuum," Phys. Rev. Lett. **107**, 183901 (2011).
21. C. W. Hsu, B. Zhen, J. Lee, S.-l. Chua, S. G. Johnson, J. D. Joannopoulos, and M. Soljac, "Observation of trapped light within the radiation continuum," Nature **499**, 188–191 (2013).
22. J. Lee, B. Zhen, S. L. Chua, W. Qiu, J. D. Joannopoulos, M. Soljačić, and O. Shapira, "Observation and differentiation of unique high-Q optical resonances near zero wave vector in macroscopic photonic crystal slabs," Phys. Rev. Lett. **109**, 1–5 (2012).

Optics EXPRESS

23. A. Kodigala, T. Lepetit, Q. Gu, B. Bahari, Y. Fainman, and B. Kanté, "Lasing action from photonic bound states in continuum," Nature **541**, 196–199 (2017).
24. S. Romano, G. Zito, S. Managò, G. Calafiore, E. Penzo, S. Cabrini, A. C. De Luca, and V. Mocella, "Surface-enhanced raman and fluorescence spectroscopy with an all-dielectric metasurface," J. Phys. Chem. C **122**, 19738–19745 (2018).
25. B. Zhen, S.-L. Chua, J. Lee, A. W. Rodriguez, X. Liang, S. G. Johnson, J. D. Joannopoulos, M. Soljačić, and O. Shapira, "Enabling enhanced emission and low-threshold lasing of organic molecules using special Fano resonances of macroscopic photonic crystals," Proc. Natl. Acad. Sci. **110**, 13711–13716 (2013).
26. E. N. Bulgakov and D. N. Maksimov, "Light enhancement by quasi-bound states in the continuum in dielectric arrays," Opt. Express **25**, 14134–14147 (2017).
27. H. M. Doeleman, F. Monticone, W. den Hollander, A. Alù, and A. F. Koenderink, "Experimental observation of a polarization vortex at an optical bound state in the continuum," Nat. Photonics **12**, 397 (2018).
28. Z. Sadrieva, K. Frizyuk, M. Petrov, Y. Kivshar, and A. Bogdanov, "Multipolar origin of bound states in the continuum," arXiv:1903.00309 (2019).
29. J. Jin, X. Yin, L. Ni, M. Soljačić, B. Zhen, and C. Peng, "Topologically enabled ultra-high-q guided resonances robust to out-of-plane scattering," arXiv:1812.00892 (2018).
30. A. C. Overvig, S. C. Malek, M. J. Carter, S. Shrestha, and N. Yu, "Selection rules for symmetry-protected bound states in the continuum," arXiv:1903.11125 (2019).
31. F. Yesilkoy, E. R. Arvelo, Y. Jahani, M. Liu, A. Tittl, V. Cevher, Y. Kivshar, and H. Altug, "Ultrasensitive hyperspectral imaging and biodetection enabled by dielectric metasurfaces," Nat. Photonics **doi.org/10.1038/s41566-019-0394-6** (2019).
32. A. Tittl, A. Leitis, M. Liu, F. Yesilkoy, D.-Y. Choi, D. N. Neshev, Y. S. Kivshar, and H. Altug, "Imaging-based molecular barcoding with pixelated dielectric metasurfaces," Science **360**, 1105–1109 (2018).
33. S. Romano, G. Zito, S. Torino, S. Cabrini, I. Rendina, G. Coppola, G. Calafiore, E. Penzo, and V. Mocella, "Label-free sensing of ultralow-weight molecules with all-dielectric metasurfaces supporting bound states in the continuum," Photonics Res. **6**, 726–733 (2018).
34. S. Romano, A. Lamberti, M. Masullo, E. Penzo, S. Cabrini, I. Rendina, and V. Mocella, "Optical biosensors based on photonic crystals supporting bound states in the continuum," Materials **11**, 1–11 (2018).
35. V. Liu and S. Fan, "S^4 : A free electromagnetic solver for layered periodic structures," Comp. Phys. Comm. **183**, 2233 – 2244 (2012).
36. G. Zito, G. Rusciano, and A. Sasso, "Enhancement factor statistics of surface enhanced raman scattering in multiscale heterostructures of nanoparticles," J. Chem. Phys **145**, 054708 (2016).
37. S. Managò, G. Zito, A. Rogato, M. Casalino, E. Esposito, A. C. De Luca, and E. De Tommasi, "Bioderived three-dimensional hierarchical nanostructures as efficient surface-enhanced raman scattering substrates for cell membrane probing," ACS Appl. Mater. Interfaces **10**, 12406–12416 (2018).
38. K. Sakoda, *Optical Properties of Photonic Crystals* (Optical Sciences, 2005).
39. Z. F. Sadrieva, I. S. Sinev, K. L. Koshelev, A. Samusev, I. V. Iorsh, O. Takayama, R. Malureanu, A. A. Bogdanov, and A. V. Lavrinenko, "Transition from optical bound states in the continuum to leaky resonances: role of substrate and roughness," ACS Photonics **4**, 723–727 (2017).
40. T. L. McMeekin, M. L. Groves, and N. J. Hipp, "Refractive indices of amino acids, proteins, and related substances," Amino Acids Serum Proteins **44**, 54–66 (1964).
41. N. Bosio, H. Šípová-Jungová, N. Odebo Länk, T. J. Antosiewicz, R. Verre, and M. Käll, "Plasmonic versus all-dielectric nanoantennas for refractometric sensing: a direct comparison," ACS Photonics http://dx.doi.org/10.1021/acsphotonics.9b00434 (2019).
42. G. G. Nenninger, M. Piliarik, and J. Homola, "Data analysis for optical sensors based on spectroscopy of surface plasmons," Meas. Sci. Technol. **13**, 2038 (2002).
43. P. Skafte-Pedersen, P. Nunes, S. Xiao, and N. Mortensen, "Material limitations on the detection limit in refractometry," Sensors **9**, 8382–8390 (2009).